An Implantable Photovoltaic Energy Harvesting System with Skin Optical Analysis

Jinwei Zhao, Yang Jiang, Man-Kay Law, Rami Ghannam, Muhammad Imran, Hadi Heidari
State Key Laboratory of Analog and Mixed‐Signal VLSI, AMSV, University of Macao, Macao, China
Microelectronics Lab (meLAB), James Watt School of Engineering, University of Glasgow, G12 8QQ, UK

***Abstract*— Medical implantable devices can use photovoltaic (PV) energy harvesting to extend battery life span and increase their performance. The power conditioning and management circuitry is essential not only to regulate the voltage requirements of the load but also optimize the output power of PV cells. However, the optical losses due to the skin and the device characteristics of the PV cells are rarely analyzed before chip fabrication. This inevitably leads to sub-optimal system performance in *in-vitro* or *in-vivo* tests owing to the varying PV output characteristics. To address this problem, we use the finite-element-method (FEM) to analyze the optical and physical performance of the PV cell under the skin, and then export the model into the p-spice simulator for circuit-level implementation. We further demonstrate a 1:2 cross-coupled DC-DC converter using pulse density modulation for load regulation control to meet the loading requirement.**

Keywords—Implantable Device, Photovoltaic Energy Harvesting, Power management circuits.

I. Introduction

The majority of implantable devices such as pacemakers, cochlear hearing aids, and neural stimulators [1] are still powered by batteries. However, this powering technique is limited by lifespan, capacity, and large size. Furthermore, the battery leakage issue is potentially harmful to the health of patients. Battery performance can be improved using alternative implantable energy harvesting techniques [2] including Radio-Frequency (RF) energy harvesters [3], Photovoltaic Cells (PVC) [4], Piezoelectric Generator (PEG) and Thermoelectric Generators (TEG). In comparison with other energy harvesting methods, implantable PV cells are advantageous for their large power density, stable output voltage, small active area and flexible stacking techniques. Besides, the power conditioning and management circuit with the Maximum Power Point Tracking algorithm can regulate the PV electrical output to meet the loading requirement while optimizing the harvested power under the same lighting condition.

Optical absorption in the skin will dominate all the losses in the PV energy harvesting system, which influences the input power to the system power conditioning circuit. According to the literature, over 90% of white light will be absorbed by skin, leaving a small proportion to be harvested by PV cells [5]. The different PV characteristics with and without skin will inevitably limit the performance of the whole system, potentially resulting in a low PV voltage and start-up problems. Consequently, it is significant to analyze the optical losses of the implantable PV cells before the circuit design and chip fabrication.

In this paper, we use the Finite-Element-Method (FEM) multiphysics simulations tool was used to evaluate the optical losses of skin and to optimize the electrical output of the PV cell. Next, the device characteristics will be exported to the circuit design software to design and optimize the power conditioning and management circuit. With the harvested energy from the implantable PV cell, we further designed a 1:2 cross-coupled switch-capacitor (SC) dc-dc converter with the Pulse Skipping Modulation (PSM) for output voltage regulation, and compare our proposed approach with the state of the art.

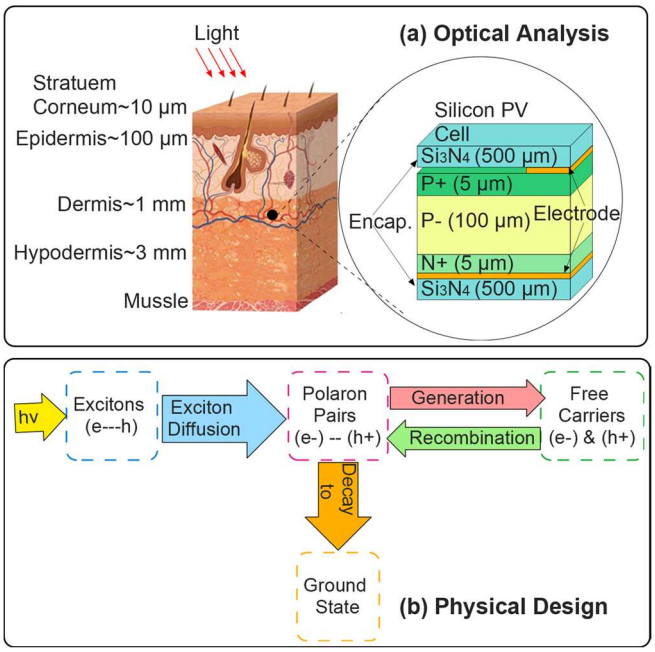

Fig. 1. The design procedure of the implantable photovoltaic energy harvesting system: (a) the optical analysis including multilayer human skins, Si_3N_4 encapsulation and Silicon PV cell. (b) the physical analysis in FEM simulation, which includes excitons, diffusions, generation and recombination.

II. Device and Circuit Design

A. PV Cell Design and Analysis

The design of implantable PV cells is divided into two parts: the optical analysis and physical analysis. The optical analysis describes the quantity of light that can reach the surface of the PV cell, while the physical analysis corresponds to how the photovoltaic power can be converted into electricity. First, the combination of skin and the PV cell can be regarded as a multilayer filter (shown as Fig. 1(a)), where the skin consists of stratum corneum, epidermis, dermis as well as the hypodermis, and the PV cell includes the semiconductor, metal electrodes and encapsulation. In general, the thickness of the stratum corneum is ~10 μm, while those of the epidermis, dermis and hypodermis are ~100 μm, 1~4 mm, and 1~6 mm, respectively [6]. When light penetrates the skin, the majority of light will be absorbed by the skin and the encapsulation, and only a small proportion will reach the implantable PV cell.

Since the skin layers are complex, it is a challenge to achieve accurate simulation using a monolayer model [7]. Beer-Lambert Law is normally applied to analyze the optical performance rapidly in the photovoltaic effect in 1D simulation. However, the poor estimation limits its usage in a

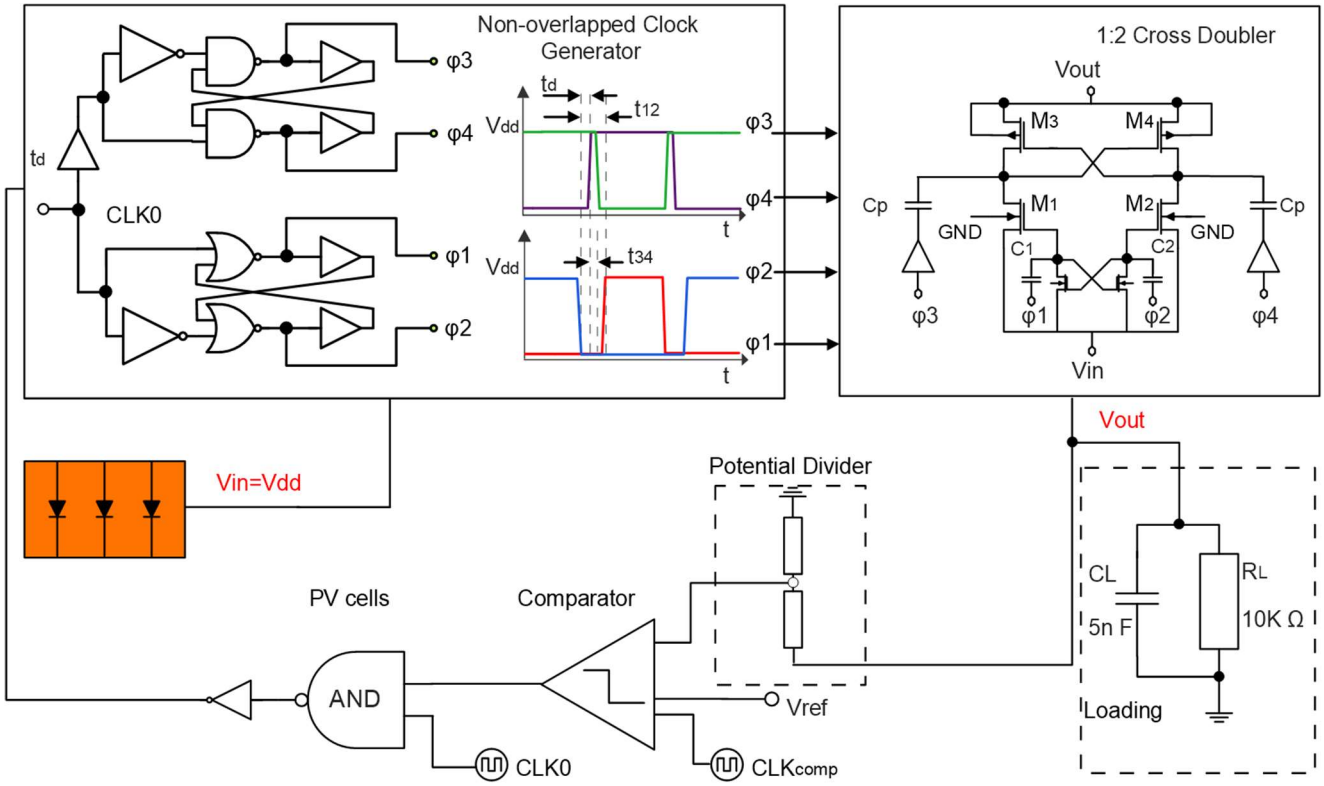

Fig. 2. The circuit implementation of the switched-capacitor DC-DC converter. The extracted PV cell characteristics from FEM is converted to the equivalent circuit model using Verilog A.

complex multilayer structure in 2D or 3D FEM simulation [8]. A better way is presenting the Maxwell Equation in Jones' Matrix to calculate the Snell's Law and estimate the optical properties:

$$\begin{bmatrix} E_{Ra} \\ B_{Ra} \end{bmatrix} = \left\{ \sum_{i=1}^{m} \begin{bmatrix} \cos\varphi_i & \left(\frac{j}{\eta_i}\right)\sin\varphi_i \\ j\eta_i \sin\varphi_i & \cos\varphi_i \end{bmatrix} \right\} \begin{bmatrix} 1 \\ \eta_m \end{bmatrix} \tag{2.1}$$

where δ_i $_i$= $2\pi \cdot N_i \cdot d_i \cdot \cos\theta_i / \lambda$ is the wave phase shift in the ith layer, N_i is the refractive index, d_i is the thickness of the ith layer, and η_i is the pseudo index in ith layer ($\eta_i = N_i \cdot \cos\theta_i$). E_{Ra} (B_{Ra}) is the ratio between the electric (magnetic) field of the transmitted light and the electric (magnetic) field of the incident light, and m is the total number of layers. The reflectance (R), transmittance (T) and absorptance (A) of light can be determined using:

$$T = \frac{4\eta_0 \, Re(\eta_m)}{(\eta_0 E_{Ra} + B_{Ra})(\eta_0 E_{Ra} + B_{Ra})^*} \tag{2.2}$$

$$A = \frac{4\eta_0 \, Re(E_{Ba} B_{Ra}^* - \eta_m)}{(\eta_0 E_{Ra} + B_{Ra})(\eta_0 E_{Ra} + B_{Ra})^*} \tag{2.3}$$

The process of physical design is shown in Fig. 1(b), which demonstrates how optical energy is converted into electrical energy. To analyze this process, we involve the poisons equations, which consist of diffusion currents, generation rate and recombination rate, to derive the following equations:

$$J_{sc} = \iiint \left| J_n(x,y,\lambda) + J_p(x,y,\lambda) \right| dxdyd\lambda \tag{2.4}$$

$$J(V) = -J_0 e^{-\frac{V}{V_T}} + J_{sc} - \frac{V + J(V)R_s}{R_{sh}} \tag{2.5}$$

where R_s and R_{sh} are the series and shunt parasitic resistances, and V_T = k·T/q is the thermal voltage. Since our simulation model is in 2D, R_s can be neglected and R_{sh} can be calculated using the IV characteristic of the device.

External Quantum Efficiency (EQE) is defined as follows:

$$EQE = \frac{hcJ_{sc}}{q\lambda P_{in}} \tag{2.6}$$

where h is the Plank constant, c is the speed of light, P_{in} is the input power flux density (AM 1.5G light intensity).

During device implementation, we optimized the PV cell performance with 5 μm thickness for the P+ layer, 100 μm thickness for the P- layer and 5 μm thickness for the N+ layer. Generally, we will design the intrinsic layer thicker than the heavily doped layer to absorb light and convert it into electricity. Intrinsic silicon suffers from the short lifetime of minority carries, while the thin heavily doped layer can enhance the lifetime of electron-hole pairs but can damage the structure of the intrinsic silicon. According to this structure, the optimal doping concentration for the P+, P- and N+ layer are 2×10^{17} cm^{-3}, 1×10^{10} cm^{-3} and 2.5×10^{16} cm^{-3}. The area of the PV cell is assumed to be 1.23 mm^2.

B. Power conditioning Circuit Design

We apply the cross-coupled switched-capacitor voltage doubler in Fig. 2 to sustain the load [9, 10]. To properly control the N-switches $M_{1,2}$, we applied a level shifter to adaptively boost the clock signals φ_1 and φ_2. Capacitors $C_{1,2}$ are for clock boosting and C_p is for voltage pumping [11], with

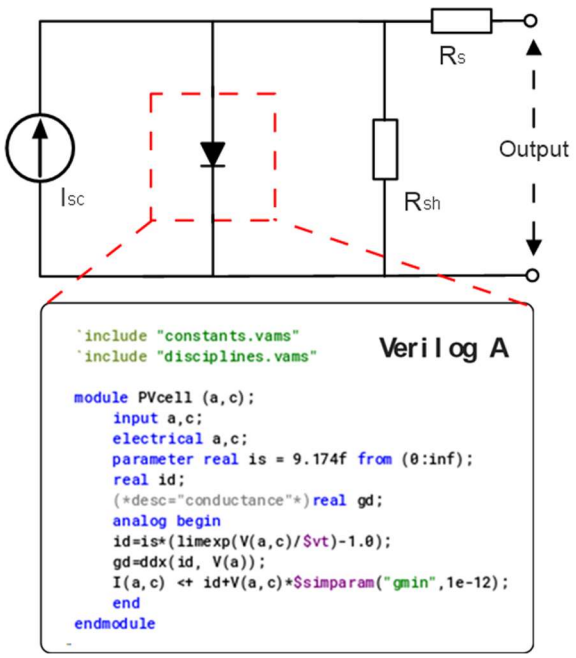

Fig. 3. The equivalent circuit of the PV cell, where the diode part is built using Verilog A.

C_p designed to be much larger than $C_{1,2}$ to reduce the conduction loss. With C_p = 5 pF, we added two parasitic capacitors in the top plate (3%) and bottom plate (5%) for estimating the parasitic loss. The input voltage (V_{in}) is supplied by two series-connected PV cells, which is a Verilog-A model based on the I-V curve from FEM simulation in COMSOL. The PV cell model in Cadence is shown in Fig. 3.

The 4-phase non-overlapping clock generator, which can reduce the reversion loss (induced by the shooting-through current in M_3 and M_4 in Fig. 2) by introducing the dead time in different switching cycles, is shown in Fig. 2. The corresponding voltage swing is from 0 to V_{in}.

In this work, we assume that the voltage requirement of the implantable device is from 1 to 2 V, with loading in the µA range [12]. Regulation is necessary to obtain a stable output voltage (V_{out}) under different loading conditions, as achieved by a comparator to form a negative feedback loop using Pulse Skipping Modulation (PSM). In PSM operation, $M_{1,2}$ and $M_{3,4}$ are driven by an external clock (CLK0 ~6.67 MHz). V_{out} is compared with the reference voltage V_{ref}; and pulses are skipped to stop pumping charge to the output if $V_{out} > V_{ref}$. The comparator is operating at CLK_{comp} ~8 MHz.

III. Results and Discussion

In the optical analysis, the skin will absorb the majority of the incident light (especially for an ultraviolet light source). To evaluate the optical loss, we apply the standard one sun condition at air mass (AM) 1.5G (global) condition, which is 1000 W/m^2. The optical results are shown in Fig. 4(a). The absorption rate for the ultraviolet light is 95% at 300 nm wavelength. Then, the absorption rate for visible light is from 40% to 60%. It is noted that the skin transmittance can be higher than 60% by using Near Infrared light (NIR). To obtain the specific wavelength for the proposed light source, we swept the incident wavelength from 400 to 1200 nm and evaluated the light generated current for each wavelength. By using Eq. 2.6, the External Quantum Efficiency (EQE) can be achieved, as shown in Fig. 4(b). By considering the optical loss from skin and encapsulation, the maximum EQE decreases from approximately 60% to 30%, and the peak wavelength shifts to 890 nm (Optimal Wavelength). The IV curves of the PV cell in different conditions is shown in Fig. 2(c). At 1000 W/m^2, the proposed PV cell can provide 377.94 µA/mm^2 of short circuit current (J_{sc}) and 0.64 V open-circuit voltage (V_{oc}), and the power conversion efficiency is approximately 19%. After considering the optical loss of the skin and encapsulation, the J_{sc} was dropped to 227.41µA/mm^2, and V_{oc} reduced to 0.62 V. Considering the implantable device must have a small volume (< 1 cm^3), we estimate the area of the proposed PV cell as 1.23 mm^2. In this case, the current density will be transferred into the current, and the PV cell is capable to extract into the Cadence model with its IV curve (Shown in Fig. 4(c)).

In the circuit design, we stacked two PV cells in series to enhance the voltage output, which can provide a 1.1 V output voltage. Fig. 5(a) shows the output voltages when the circuit is regulated by different V_{ref}. Fig. 5(b) shows the efficiencies according to the voltage regulation, which is from 20% to 84%. The relative powers are shown in Fig. 5(c), which includes the power (P_{out}) supplied by the PV cells and power (P_{out}) supplying to the load. The output powers vary from 200 µW

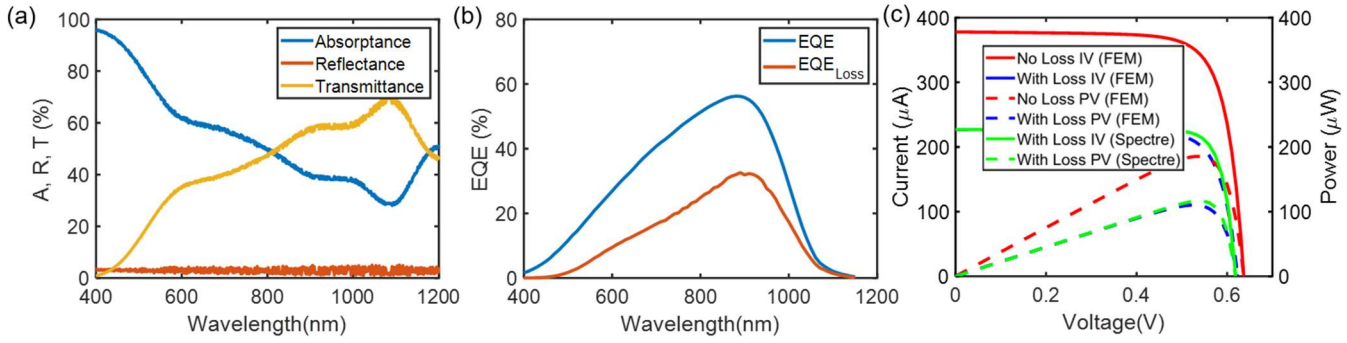

Fig. 4. Simulation results of the implantable photovoltaic energy harvesting system: (a) The optical analysis considering the multi-layer structure of the human skin including stratum corneum, epidermis, dermis and hypodermis, as well as the optical loss of the Si_3N_4 encapsulation. (b) The EQE of the PV cells under different illumination condition, considering the optical loss from skin and encapsulation (Red line), cell only (Blue line). (c) The IV curves (Current vs. Voltage) and PV curves (Power vs. Voltage) in both FEM simulation and Cadence simulation (Spectre) including IV curve (Red solid line) and PV curve (Red dot line) in the FEM simulation without optical loss from skin and encapsulation, IV curve (Blue solid line) and PV curve (Blue dot line) in the FEM simulation with optical loss from skin and encapsulation as well as IV curve (Green solid line) and PV curve (Green dot line) in the Spectre simulation with optical loss from skin and encapsulation.

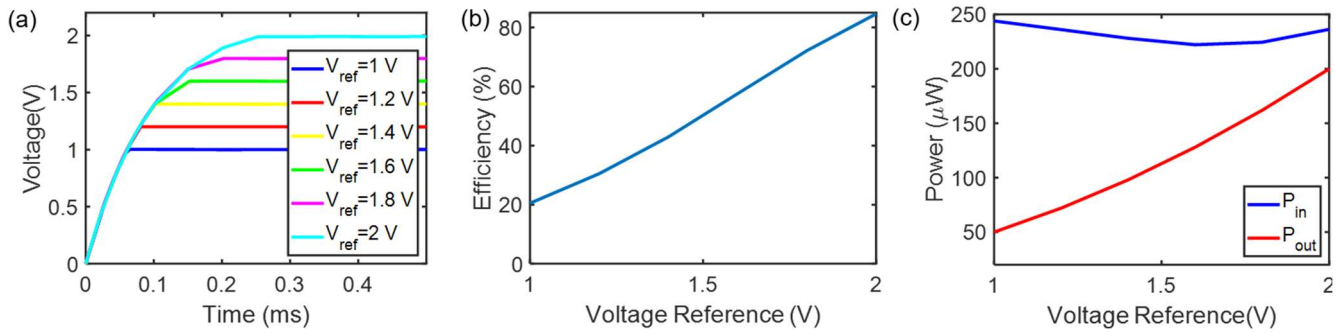

Fig. 5. (a) The regulated output voltage using V_{ref} from 1V to 2V. (b) The power conversion efficiency according to different V_{ref}. (c) The input power (PV cell) and output power (Load) in the system vs V_{ref}. The loading capacitor and loading resistor in the circuit are 5 nF and 10 kΩ respectively.

to 50 μW, which is feasible to supply low power consumption such as Pacemakers (10s μW) and the retinal stimulator (100s μW) [12].

We compared our work with the state of the art [13-15], which is shown in Table 1. Our work achieved a higher PV cell efficiency than the literature and can provide higher harvested energy after concerning optical loss. In Chang *et al.* work, the efficiency of the PV cell is not shown directly. Instead, a harvested power of 50 μW at 1200 lux is provided [12]. As the power source is not shown in the paper, it is impossible to calculate the efficiency with the data given.

IV. Conclusion

Our implantable PV cell can achieve 19% efficiency and provide 110 μW to the implantable loading device. The Voc is 0.6 V which is larger than the majority of the PV cells in the market. The energy harvesting circuit can obtain an end to end efficiency 84% to 20% with different V_{out} (1 V – 2 V). This emerging FEM to the circuit can help the device and circuit designer to investigate the harvested power from a different type of implantable PV cells before the chip design and the fabrication.

TABLE I
Performance Comparison Summary

	This Work	TBioCAS [13]	TBioCAS [14]	TCAS-II [15]
PV Eff.	18%	16%	-	-
Light	890 nm	850 nm	700-1000 mm	-
Skin	>4 mm	4.5 mm	3 mm	-
Encap.	Si_3N_4	-	-	-
Tech.	0.18 μm	0.18 μm	0.18 μm	0.18 μm
Circuit Eff.	84%	67%	23%	68.3 %
V_{out}	2 V	1.2 V	-	0.425 V
Regulation	Yes	No	No	No

References

[1] R. Das, F. Moradi, and H. Heidari, "Biointegrated and Wirelessly Powered Implantable Brain Devices: A Review," *IEEE Transactions on Biomedical Circuits and Systems,* pp. 1-1, Jan. 2020.

[2] J. Zhao *et al.*, "Self-Powered Implantable Medical Devices: Photovoltaic Energy Harvesting Review," *Advanced Healthcare Materials,* p. 2000779, July 2020.

[3] K. Agarwal, R. Jegadeesan, Y.-X. Guo, and N. V. Thakor, "Wireless Power Transfer Strategies for Implantable Bioelectronics," *IEEE Reviews in Biomedical Engineering,* vol. 10, pp. 136-161, Mar. 2017.

[4] J. Zhao, R. Ghannam, M. K. Law, M. A. Imran, and H. Heidari, "Photovoltaic Power Harvesting Technologies in Biomedical Implantable Devices Considering the Optimal Location," *IEEE Journal of Electromagnetics, RF and Microwaves in Medicine and Biology,* vol. 4, no. 2, pp. 148 - 155, Aug. 2019.

[5] L. Lu *et al.*, "Biodegradable Monocrystalline Silicon Photovoltaic Microcells as Power Supplies for Transient Biomedical Implants," *Advanced Energy Materials,* vol. 8, no. 16, p. 1703035, June 2018.

[6] A. N. Bashkatov, E. A. Genina, and V. V. Tuchin, "Optical Properties of Skin, Subcutaneous, and Muscle Tissues: A Review," *Journal of Innovative Optical Health Sciences,* vol. 4, no. 01, pp. 9-38, Jan. 2011.

[7] J. Zhao, K. O. Htet, R. Ghannam, M. Imran, and H. Heidari, "Modelling of Implantable Photovoltaic Cells Based on Human Skin Types," in *2019 15th Conference on Ph. D Research in Microelectronics and Electronics (PRIME)*, 2019: IEEE, pp. 253-256.

[8] X. Li, N. P. Hylton, V. Giannini, K. H. Lee, N. J. Ekins-Daukes, and S. A. Maier, "Multi-dimensional Modeling of Solar Cells with Electromagnetic and Carrier Transport Calculations," *Progress in Photovoltaics: Research and Applications,* vol. 21, no. 1, pp. 109-120, Jan. 2013.

[9] J. Wu *et al.*, "Fully Integrated High Voltage Pulse Driver Using Switched-Capacitor Voltage Multiplier and Synchronous Charge Compensation in 65-nm CMOS," *IEEE Transactions on Circuits and Systems II: Express Briefs,* vol. 66, no. 10, pp. 1768-1772, June 2019.

[10] K. Oo Htet, R. Ghannam, Q. H. Abbasi, and H. Heidari, "Power Management Using Photovoltaic Cells for Implantable Devices," *IEEE Access,* vol. 6, pp. 42156 - 42164, Aug. 2018.

[11] Z. Luo, L. Yu, and M. Ker, "An Efficient, Wide-Output, High-Voltage Charge Pump With a Stage Selection Circuit Realized in a Low-Voltage CMOS Process," *IEEE Transactions on Circuits and Systems I: Regular Papers,* vol. 66, no. 9, pp. 3437-3444, July 2019.

[12] B. Shi, Z. Li, and Y. Fan, "Implantable Energy-Harvesting Devices," *Advanced Materials,* vol. 30, no. 44, p. 1801511, July 2018.

[13] Z. Chen, M.-K. Law, P.-I. Mak, and R. P. Martins, "A Single-Chip Solar Energy Harvesting IC Using Integrated Photodiodes for Biomedical Implant Applications," *IEEE Transactions on Biomedical Circuits and Systems,* vol. 11, no. 1, pp. 44-53, Feb. 2017.

[14] S. Ayazian, V. A. Akhavan, E. Soenen, and A. Hassibi, "A Photovoltaic-Driven and Energy-Autonomous CMOS Implantable Sensor," *IEEE Transactions on Biomedical Circuits and Systems,* vol. 6, no. 4, pp. 336-343, Aug. 2012.

[15] M. Chang and S. Liu, "An Indoor Photovoltaic Energy Harvester Using Time-Based MPPT and On-chip Photovoltaic Cell," *IEEE Transactions on Circuits and Systems II: Express Briefs,* pp. 1-1, Feb. 2020.